Bioresource Technology Reports 33 (2026) 102531

Contents lists available at ScienceDirect

Bioresource Technology Reports

journal homepage: www.sciencedirect.com/journal/bioresource-technology-reports

Banana crop biomass-derived chemically activated filters for concurrent removal of particulate matter and volatile organic compounds

Yumara Martín-Cruz [a], Pablo Bordón [a,*], Teresa Saura-Cayuela [b], Mario Monzón [a], Elisenda Pulido-Melián [b,*]

[a] Integrated and Advanced Manufacturing Research Group, University of Las Palmas de Gran Canaria, 35017 Las Palmas, Spain
[b] Photocatalysis and Spectroscopy for Environmental Applications Group (FEAM), Institute of Environmental Studies and Natural Resources (i-UNAT), University of Las Palmas de Gran Canaria, 35017 Las Palmas, Spain

ARTICLE INFO

Keywords:
Air pollution
Biomass valorization
Air filtration
Particle capture efficiency
Gas adsorption
Sustainable materials

ABSTRACT

Air pollution caused by particulate matter (PM) and volatile organic compounds (VOCs) poses a critical threat to public health, contributing to millions of premature deaths each year. This growing problem underscores the urgent need for sustainable and efficient air filtration systems. This study presents the development of biodegradable filters based on biomass from banana cultivation in the Canary Islands, a residual and abundant natural resource, enabling dual valorization by using the cellulose as a structural matrix and the same biomass to produce activated carbon. Filters were fabricated via freeze-drying and incorporated activated carbon produced through chemical activation with H_3PO_4 or KOH at varying concentrations. Comprehensive characterization was conducted using scanning electron microscopy, Fourier-transform infrared spectroscopy, and porosity analysis, in addition to performance testing for both PM filtration (0.3–10 μm) and toluene gas adsorption. Filters with 10 % H_3PO_4-activated carbon showed the highest PM filtration efficiency, reaching 95 % for particles $\geq$0.5 μm and exceeding 90 % for submicron particles, with cumulative efficiencies over 80 % for $PM_{2.5}$ and PM_1. These results were attributed to higher surface area and internal porosity, though accompanied by an increased pressure drop (~800 Pa). In contrast, KOH-activated carbon demonstrated superior toluene adsorption capacity, remaining unsaturated for up to 350 min, due to its surface functional groups' greater affinity for non-polar compounds. The findings reveal a functional complementarity between both activation methods, allowing for the design of application-specific or dual-layer multifunctional filters. This work supports the use of banana biomass as a sustainable alternative to synthetic materials in air pollution control technologies.

1. Introduction

Air pollution is a major global concern, causing around 7 million premature deaths per year (NSW Government, 2025). While outdoor pollution comes from traffic, industry, or waste incineration, indoor air quality is often worse (Buyukada-Kesici et al., 2021), as people spend over 90 % of their time indoors. Sources include cleaning, cooking with kerosene or charcoal, infiltration of outdoor pollutants, secondary chemical reactions (Saraga et al., 2023; Vardoulakis et al., 2020), and emissions from furniture, paints, and wall coverings (Li et al., 2020; Mata et al., 2022). These pollutants generate particulate matter (PM), together with gaseous compounds, that pose significant risks to human health. Consequently, there is growing interest in indoor air purification strategies capable of simultaneously addressing both particulate and gaseous pollutants within a single system, while meeting environmental sustainability requirements, for instance through the use of innovative filtration materials derived from renewable and waste-based resources. PM is a complex mixture of chemical and biological compounds that adversely affect human health, causing cardiovascular problems (Kanagasabai et al., 2022; Raju et al., 2023), respiratory diseases (Radbel et al., 2024), sleep disorders (Yu et al., 2021), bone and skin lesions (Adami et al., 2022; Park et al., 2022), and damage to the brain, digestive, and reproductive systems (Arias-Pérez et al., 2020; Chew et al., 2020; Pang et al., 2023). PM is also classified by particle size into PM_{10} (particles with an aerodynamic diameter less than 10 μm), $PM_{2.5}$ (< 2.5 μm), PM_1 (< 1 μm), and $PM_{0,3}$ (< 0.3 μm), with smaller particles causing greater harm (Radbel et al., 2024) due to deeper penetration into the human body and bloodstream, especially ultrafine particles

---

* Corresponding authors.
E-mail addresses: pablo.bordon@ulpgc.es (P. Bordón), elisenda.pulido@ulpgc.es (E. Pulido-Melián).

https://doi.org/10.1016/j.biteb.2025.102531
Received 25 July 2025; Received in revised form 18 December 2025; Accepted 29 December 2025

from combustion (Mannan and Al-Ghamdi, 2021). Due to these risks to human health, implementing measures to reduce pollution, such as air purification systems, is essential. Filtration is the most common technique for PM removal (Mata et al., 2022), typically using fibrous filters due to their high capture efficiency and simple structure. However, these filters often have high pressure drops, increasing energy costs. Common materials like fiberglass or fossil-fuel derivatives are expensive and non-biodegradable. Consequently, research has focused on biodegradable and recyclable alternatives, such as cellulose, which has a large specific surface area and high potential for air filtration (Gough et al., 2021; Rana et al., 2023).

Among gases, volatile organic compounds (VOCs) are particularly important due to their carcinogenic and teratogenic effects, as well as chronic headaches, respiratory diseases (asthma, COPD), and increased risk of miscarriages (Li et al., 2020; Sadegh et al., 2024). The most harmful VOCs are the BTEX group (benzene, toluene, ethylbenzene, xylene), because of their high stability and high accumulation in the human body. The primary removal technique for VOCs is adsorption (Mata et al., 2022), which is also effective for fine particles. This method retains gas molecules on a porous solid, called an adsorbent, and its low cost allows recovery and reuse of both the VOCs and the adsorbent (Li et al., 2020; Sadegh et al., 2024). Activated carbon (AC) is among the most widely used adsorbents (Ioannidou and Zabaniotou, 2007; Sadegh et al., 2024) due to its high surface area (Brunauer-Emmet-Teller surface $>700\ m^2 \cdot g^{-1}$), significant porosity, and abundant functional groups.

The textural behavior of ACs, however, is not determined solely by the activation step: it strongly depends on the nature of the biomass precursor (cellulose, hemicellulose, lignin, and ash content), the choice and ratio of activating agent (e.g., KOH, H_3PO_4, $ZnCl_2$), and the overall production route (one-step vs. two-step, physical vs. chemical activation, and pretreatments). Biomass precursors with higher lignin or ash contents tend to favour meso- and macropore formation, whereas cellulose-rich fibers promote microporosity. Among chemical activating agents, KOH is widely reported to develop very high surface areas (often exceeding 2000–3000 $m^2\ g^{-1}$ under optimized conditions) by extensive alkali etching and micropore generation, reaching some of the highest BET values reported for lignocellulosic carbons through chemical activation (Kundu et al., 2024; Mostazo-López et al., 2019). In contrast, H_3PO_4 activation typically yields materials with moderate to high surface areas (ranging from ~450 up to ~2800 $m^2\ g^{-1}$ depending on precursor and conditions), often with a broader pore size distribution including significant mesoporosity and enhanced surface functionalities (Neme et al., 2022). These differences reflect the distinct mechanisms of pore development: KOH promotes extensive carbon etching and microporosity, whereas H_3PO_4 facilitates dehydration and cross-linking reactions that favour a mix of micro- and mesopores (Chew et al., 2023; Lin et al., 2022). These parameters collectively control pore size distribution, specific surface area and surface chemistry thus critically influence the material's suitability for VOC capture and reuse. Recent studies show that different lignocellulosic precursors produce carbons with markedly distinct textures and adsorption performances (Tonu et al., 2024), while single versus mixed activators can favour ultramicroporosity or mesoporosity (Zhang et al., 2025). Complementary to gas-phase adsorption, cellulose-based materials show outstanding particulate filtration performance. Nanocellulose filters capture >97 % of ultrafine particles (0.1–0.3 μm) with low pressure drop (Sawatdee et al., 2025), while spider-web-like dual-network cellulose fibers reach >99 % efficiency for ultrafine particles with low air resistance and high biodegradability (Nie et al., 2025). Hybrid filters combining cellulose with natural fibers (e.g., basalt) improve chemical and thermal resistance as well as fire-retardant properties (Atalie et al., 2024). Functionalized cellulose filters have also shown high efficiency: nanofibrils mixed with bamboo activated carbon, polyethylenimine, and ammonium polyphosphate achieve >98 % for $PM_{2.5}$ (Nie et al., 2025), cellulose acetate with nanoclays effectively adsorbs polyaromatic hydrocarbons from rice smoking (Fallah et al., 2024), and cellulose nanofibrils/Na-montmorillonite composites capture up to 96 % of PM2.5 and 81.97 mg/g of formaldehyde (Cai et al., 2024).

Among raw materials for cellulose production, agricultural waste has gained importances in the last decade due to low cost and high lignocellulosic content (Cui et al., 2025; Hu et al., 2023; Tiwari and Sanjog, 2025). This waste is also a valuable source of activated carbon (Kakom et al., 2024; Sujiono et al., 2022). Banana crop residues—including pseudostem, rachis and peels— are widely used (Cordeiro et al., 2024; Rahman et al., 2024; Sreńscek-Nazzal et al., 2024). Using these residues valorizes waste and helps manage the environmental problem of large-scale disposal. In the Canary Islands, where banana is the main crop, annual production reached 467,256 kg in 2023 (Asprocan, 2024), generating around 17 million kg of waste per year. Unlike crops such as vineyards or potatoes, each banana plant produces fruit once and leaves a non-usable pseudostem with high cellulose content, averaging ~25 kg per plant, highlighting its potential as a biomass source.

This research aims to manufacture and validate composite air filters using cellulose fibers and AC derived from banana pseudostem waste via freeze-drying technique. The AC was obtained using two different activation agents: phosphoric acid and potassium hydroxide. First, the capture efficiency of four particles size ranges ($PM_{10\text{–}0.3}$, $PM_{2.5\text{–}0.3}$, $PM_{1\text{–}0.3}$ and $PM_{0.3}$) and their pressure drops were evaluated. Next, toluene adsorption was studied as a representative VOC. Developing high-efficiency, multifunctional filters from a single biomass for both the matrix and AC enables simultaneous removal of particulate matter and VOCs. This strategy could advance the Canary Islands' air purification industry, provide a sustainable solution for agricultural residues, promote the circular economy, and produce a commercially scalable product.

2. Materials and methods

2.1. Obtaining and treatment of banana crop pulp biomass

The process carried out in this study to obtain cellulose pulp consisted of three main stages. Firstly, cellulose fibers were extracted from the pseudostem of the banana tree (Dwarf Cavendish variety) using an automated decorticating machine designed by the Integrated and Advanced Manufacturing Research Group of the University of Las Palmas de Gran Canaria and patented in conjunction with the company Celulosa de Levante S.A. (Monzón, 2014). During this process, the pseudostem leaves were mechanically scraped along their length (≈0.5 m) using two scraper systems operating with linear and rotational movements. The recovery efficiency of banana fibers was approximately 51 %, calculated as the ratio of extracted fiber mass to the total available fiber content. In terms of overall yield, the extracted fibers corresponded to about 0.8 % of the total pseudostem weight. In previous works (Martín-Cruz et al., 2024), FTIR spectra of the original fiber confirmed its lignocellulosic composition, which typically contains around 63 % cellulose (Fuqua et al., 2012; Jawaid and Abdul Khalil, 2011).

Secondly, the extracted fibers were treated using NaOH (10 %) and deionized water, catalyzed with anthraquinone (soda-anthraquinone method), for 2.5 h at 160 °C, resulting in raw pulp. It was then washed with abundant water and dried at room temperature. During this process, a delignification of the fibers occurred, resulting in the removal of approximately 70 % of the lignin content. To further remove the remaining lignin and hemicelluloses, the cellulose pulp obtained in the previous stage was subjected to a bleaching process, which involved the addition of 160 mL of $NaClO_2$ 0.3 M per gram of pulp. The pH was adjusted to approximately 4 by adding 2 mL of glacial acetic acid. The reaction was carried out for 1 h at 70 °C with slight magnetic stirring. Once the reaction was complete, the bleached pulp was filtered under vacuum using a Büchner funnel, washed until the wash water reached a neutral pH, and then dried at 35–40 °C in an oven for 24 h. Finally, the bleached pulp was ground using a ZM 200 ultra-centrifugal mill (Retsch GmbH, Haan, Germany), equipped with a 0.5 mm sieve. As a result, a more homogeneous and finer pulp was obtained, which was used in the manufacture of air filters. Fig. 1 shows a schematic representation of these mechanical and chemical processes.

The yield obtained in the first lignin removal with soda-anthraquinone was 0.8 kg of cellulose raw pulp per kg of fed cellulose fiber. After the bleaching process (lignin removal with NaClO2), a very low mass difference was obtained, with a yield of around 90 % of bleached pulp.

The standardized sequential extraction procedure allowed for the quantification and selective removal of lignin and hemicelluloses, leading to the isolation of a highly purified cellulose fraction. As shown in Fig. S1 (Supplementary Material), the final treated pulp exhibited a cellulose content of 81.31 % and a hemicellulose content of 1.77 %, corresponding to approximately 98 % cellulose within the holocellulose fraction. This represents a significant increase compared with the initial cellulose content of the original fiber, confirming the effective removal of non-cellulosic components during the purification process. These results are consistent with the FTIR spectra of the treated material, where the progressive attenuation of the characteristic aromatic absorption bands of lignin further supports the high purity of the cellulose used in the filter fabrication.

2.2. *Obtaining activated carbon*

2.2.1. *Preparation of the pseudostem core*

The synthesis of the AC was performed using the inner core of the pseudostem due to its lower and less usable fiber content, making it a good alternative source of organic matter. After removing the pseudostem leaves, the core was cut, washed with abundant water, and frozen for storage. Upon defrosting, the core was pressed and dried in an oven at 105 °C for 24 h. The freezing and defrosting process facilitated enhanced water removal and reduced the drying time. Finally, the dried core was shredded using a Fritsch PULVERISETEE 11 shredder (Fritsch GmbH, Idar-Oberstein, Germany) followed by sieving with an Endecotts OCTAGON 200 electromagnetic sieve shaker (Endecotts Ltd., London, UK), selecting a particle size range of 125–250 μm. Pseudostem core characterization, including chemical composition, SEM and EDX analysis, FTIR, and porosity measurements, is included in the Supplementary Material.

2.2.2. *Activation process*

The second stage in obtaining AC from the sieved core was the activation process, which was carried out using chemical methods. In this study, two different activating agents were used: phosphoric acid and potassium hydroxide. The optimized procedure varied slightly for each activator and is detailed in Table 1.

2.2.3. *Carbonization and purification processes*

The dry residues were carbonized using a tube furnace. In the case of activation with H_3PO_4, a first heating ramp was conducted at 5 °C · min^{-1} up to 200 °C for 2 h, followed by a second heating ramp at 5 °C · min^{-1} up to 600 °C for 3 h. In the case of the activation with KOH, the carbonization process was carried out with a heating ramp of 5 °C ·

Table 1
Activation process according to the activator used.

	Activation using H_3PO_4	Activation using KOH
Reactive	Dissolution of a 30 % (v/v) H_3PO_4 solution (ENSURE MERCK, 85 %, 1.71 g · mL^{-1})	KOH solid (SIGMA ALDRICH, 90 %) in 25 mL of deionized water
Activator biomass ratio	5 mL: 1 g	3 g: 1 g
Mixing	Orbital shaking for 24 h at 240 rpm	Orbital shaking for 48 h at 240 rpm
Oven drying	70 °C for 24 h to remove water, followed by 170 °C for 24 h to remove the activator.	80 °C for 48 h

Fig. 1. Mechanical and chemical processes for obtaining cellulose pulp from banana pseudostem.

min^{-1} up to 600 °C for 3 h. In both cases, the nitrogen flow rate was maintained at 140 $L\cdot min^{-1}$. The obtained carbon was washed using a Soxhlet extractor, with 4 cycles of 10 h each. Finally, the carbon was dried in an oven at 105 °C for 24 h and sieved using a 20 μm mesh sieve.

Following the activation, carbonization, and purification process, a yield of 0.35 g of AC H_3PO_4 per g of pseudostem core was obtained. In the KOH activation process, the yield was slightly lower, corresponding to 0.25 g AC per g of pseudostem core.

2.3. Material characterization

Chemical characterization of the cellulose raw pulp was performed following the procedure described by (Martín-Cruz et al., 2024), while the characterization of the pseudostem core is provided in the Supplementary Material.

Thermogravimetric analysis (TGA) of both raw and bleached cellulose pulp was conducted using a NETZSCH STA 449 Jupiter thermal analyzer (NETZSCH-Gerätebau GmbH, Selb, Germany) in the range of 40–900 °C, with a heating rate of 40 $°C\cdot min^{-1}$ under an inert nitrogen atmosphere (flow rate: 20 $mL\cdot min^{-1}$). Fourier Transform Infrared Spectroscopy (FTIR) was carried out using a Thermo Scientific infrared spectrophotometer (Thermo Fisher Scientific Inc., Waltham, MA, USA) within 400–4000 cm^{-1}, at a resolution of 4 cm^{-1} and 32 scans. Discs were prepared by mixing the pulp samples with KBr and pressing them at approximately 2 tons. Elemental analysis was performed with a TRUSPEC MICRO analyzer (LECO Corporation, USA) to determine the percentage composition of carbon, hydrogen, nitrogen, and sulfur in the raw and bleached cellulose pulps, as well as in the activated carbon.

To evaluate the specific area and pore size distribution of the AC, nitrogen adsorption–desorption measurements were carried out using a 3P Instruments Model 300 analyzer (3P Instruments GmbH, Odelzhausen, Germany). The specific surface area was determined by the Brunauer-Emmett-Teller (BET) method, while the total pore volume was obtained from the amount of adsorbed nitrogen at a relative pressure of 0.99. Micropore volume was estimated from the t-plot using the Boer equation, and mesopore volume was derived using the Barrett–Joyner–Halenda (BJH) method in combination with the Boer equation.

Scanning Electron Microscopy (SEM) images were acquired using a Hitachi TM3030 microscope (Hitachi High-Tech Corporation, Tokyo, Japan) operating at 15 kV. Prior to imaging, samples were Au/Pd-coated using a Quorum SC7620 mini sputter coater (Quorum Technology Ltd., Laughton, UK. Semi-quantitative surface elemental analysis was also performed using an energy-dispersive X-ray (EDX) detector integrated into the SEM equipment.

The detailed chemical and physical characterization data of the raw and bleached cellulose pulps, the pseudostem core, and the elemental analysis results are provided in the Supplementary Material.

2.4. Manufacture of composite filters

Composite filters of cellulose pulp and AC, with a grammage of 160 $g\cdot m^{-2}$, were manufactured using the freeze-drying technique. This technique for manufacturing foamy filters has been evaluated in previous studies (Martín-Cruz et al., 2024), achieving high particle retention efficiencies and acceptable pressure drop, compared to other techniques evaluated such as vacuum filtration or pressing. On the other hand, among the different grammages evaluated, the 160 $g\cdot m^{-2}$ compositions showed the best results and good manufacturability.

To obtain filters for particle filtration (Fig. 2), the following procedure was carried out: 0.23 g of bleached material was homogenized in a volume of deionized water using magnetic stirring for 5 days. After that time, 5 and 10 wt% of AC (relative to the pulp) was added, and the mixture was magnetically stirred for an additional 24 h. Finally, the resulting suspension was poured into a Petri dish (diameter of 51 mm) and placed in a freeze-dryer for 3 days. Freeze-drying was carried out at −52.7 °C and under vacuum (0.03 mbar). For gas adsorption filters, the same procedure was carried out using 0.33 g of bleached pulp and 5 wt% of AC.

For comparative purposes, two commercial materials were used. For the particle capture tests, a standard commercial carbon filter designed for $PM_{2.5}$ particle filtration (typically used in respiratory masks) was employed. This filter consists of five nonwoven layers: four outer layers made of polypropylene and one inner layer impregnated with AC (70 $g\cdot m^{-2}$). For the adsorption tests, commercial activated carbon Norit SA2 (Cabot Norit Nederland B.V.) was used.

2.5. Test instruments

2.5.1. Particle filtration testing equipment

To study the particle retention of the filters, the capture efficiency and pressure drops were assessed. For this, the testing equipment shown in the schematic of Fig. S3 of the Supplementary Material was assembled, based on a similar configuration developed by the Massachusetts Institute of Technology (MIT) (Herzog et al., 2022). Di-ethyl-hexyl-sebacate (DEHS) aerosol was selected in accordance with UNE-EN 13274–7:2020 and other international filter testing standards (ISO 16890, EN 1822/ISO 29463). It generates stable aerosols with size distributions close to the most penetrating particle size (0.3 μm) and allows the production of high particle concentrations in the 0.3–2 μm range, which is particularly relevant given their adverse effects on human health.

Particle counting was performed both upstream and downstream using an optical particle sizer (OPS) model 3330 (TSI, Minnesota, USA), with a measuring duration of 10 min at both the inlet and the outlet. The particle size range considered was 0.3–10 μm, with particle concentration and size distribution measured at a resolution of <5 %, divided into

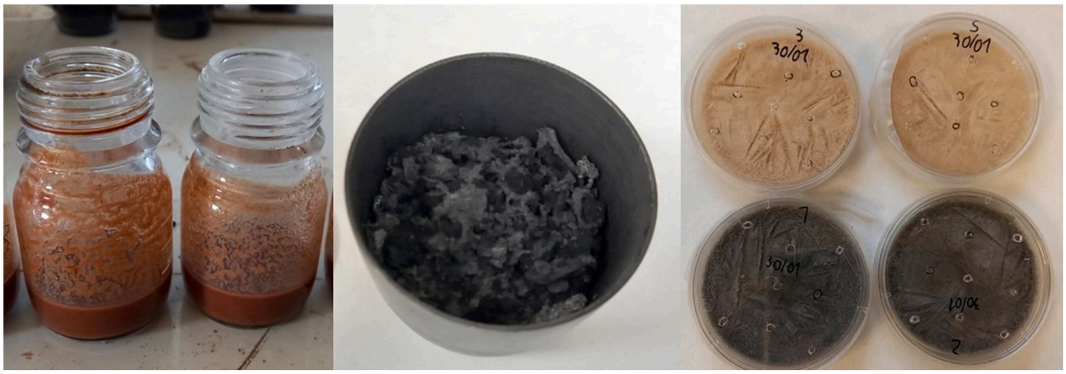

Fig. 2. Manufacturing of activated carbon filters: mixing and activation (left); Carbon carbonization (center); Freeze-drying of filters with and without activated carbon (right).

16 channels, in accordance with ISO 21501-4:2018 (Determination of particle size distribution-Single particle light interaction methods-Part 4: Light scattering airborne particle counter for clean spaces. Amendment 1). Capture efficiency was then calculated as the percentage ratio of retained particles to the total particles for four particle size ranges: $PM_{10–0.3}$, $PM_{2.5–0.3}$, $PM_{1–0.3}$, and $PM_{0.3}$.

The test system generates a constant and stable aerosol flow using an ATM 221 generator (Topas GmbH, Dresden, Germany) at 0.5 bar inlet pressure. For measuring the concentration and size distribution of particles upstream of the filter, the control valves were manually adjusted so that a fraction of the aerosol flow (1 L·min^{-1}) was drawn into the OPS device and subsequently returned to the mainstream, which then continued toward the inlet of the filter housing located at its upper section. An isokinetic sampler ensured that a representative sample was collected. The filter holder was manufactured from PVC in the laboratory with a passage diameter of 31.8 mm, allowing an aerosol flow rate of 4.5 L · min^{-1}, controlled using a flow meter and rotameters, corresponding to a face velocity of approximately 9.4 cm/s. The aerosol flow passed through the filter, positioned in the middle section of the filter housing and tightly sealed by two O-rings pressing it against the closure plates of the holder. After passing through the filter, the aerosol exited the lower part of the housing. A Belimo 22ADP-184 differential pressure sensor (Belimo, Madrid, Spain) measured the pressure upstream and downstream of the filter to calculate the pressure drop (filter flow resistance). The filtered aerosol was then released to the environment through the outlet.

To measure the filtered aerosol, the system valves were repositioned so that the entire generated flow was directed to the filter inlet. After filtration, the aerosol was directed to the isokinetic sampler, allowing a flow of 1 L·min^{-1} to be drawn into the OPS for measuring particle concentration and size distribution downstream of the filter. After measurement, this portion of the aerosol, together with the remaining flow, was discharged to the atmosphere. A detailed flow diagram and system configuration are provided in Fig. S6 of the Supplementary Material.

2.5.2. *Gas adsorption testing equipment*

To analyze the gas adsorption properties of the developed filters, the gas testing system shown in Fig. 3 was assembled. A mixture of toluene (99.95 % N_2, X10A, Air Products), with a concentration of 500 ppm_y and a flow rate of 4 mL·min^{-1}, and nitrogen (99.9999 % Nitrogen 6.0, Linde), with a flow rate of 400 mL·min^{-1}, were prepared. A flow rate of 20 mL·min^{-1} of the gaseous mixture was passed through the filter holder, a glass tube with an inner diameter of 2 mm, using a mass flow controller, corresponding to a face velocity of approximately 10.6 cm/s, which is within the range commonly used in standard filter testing protocols. Fourteen 2 mm diameter mini filters (the maximum number that could be extracted) were obtained from each original filter by means of a hole punch and inserted as filler into the glass tube. Preliminary tests with alternative support systems resulted in leaks and poor reproducibility for toluene adsorption, so a simple glass tube was used. The filters are highly porous and soft, so compression was minimized to preserve surface area. The mini filters were inserted with a snug fit against the tube walls; given their high intrinsic porosity relative to any small gaps, wall effects or channeling are considered negligible. This setup allowed uniform gas flow and reproducible measurements. The outflow from the filter holder is directed to a gas chromatograph (GC2010 Shimadzu, Kyoto, Japan) continuously, injected every 8 min through an injection valve. For the detection and quantification of toluene, the chromatograph is equipped with a flame ionization detector and a Zebron ZB-WAX chromatographic column (Phenomenex Inc., California, USA).

3. Results and discussion

3.1. *Activated carbon characterization*

3.1.1. *Scanning Electronic Microscopy and elemental analysis*

The activation process with H_3PO_4 resulted in an AC consisting of particles with irregular contours and rather rough surfaces. For activation with KOH, a more agglomerated structure with multiple hollows, resembling a honeycomb, was observed (Fig. 4). According to the elemental analysis obtained with EDX technique (Fig. 5), some particularities were observed. The percentage composition of phosphorus in AC H_3PO_4 and potassium in AC KOH were caused by the activation agent; however, potassium was also detected in the EDX analysis of the pseudostem core, therefore, the presence of this element may be due to the nature of the biomass itself. The percentage concentrations were rather low, possibly due to impurities remaining despite successive washes for activation. Similarly, silicon and magnesium were also identified in the raw biomass. Finally, the presence of aluminum and sulfur was detected in AC KOH but was not found in the EDX analysis of the pseudostem core. The possible causes could be punctual contamination of the carbon in the activation process or the presence of these elements in the pseudostem core, although they were not identified in the EDX analysis because the concentrations were very low, as in the case of the carbon.

3.1.2. *Fourier Transform Infrared spectroscopy*

The FTIR spectrum of the AC treated with H_3PO_4 (Fig. 6, spectrum A) exhibits a higher complexity in terms of surface functional groups. A broad absorption band around 3400 cm^{-1} is attributed to stretching vibrations of the hydroxyl groups, indicating the presence of residual moisture as well as hydrogen bonding with phenolic groups. The band

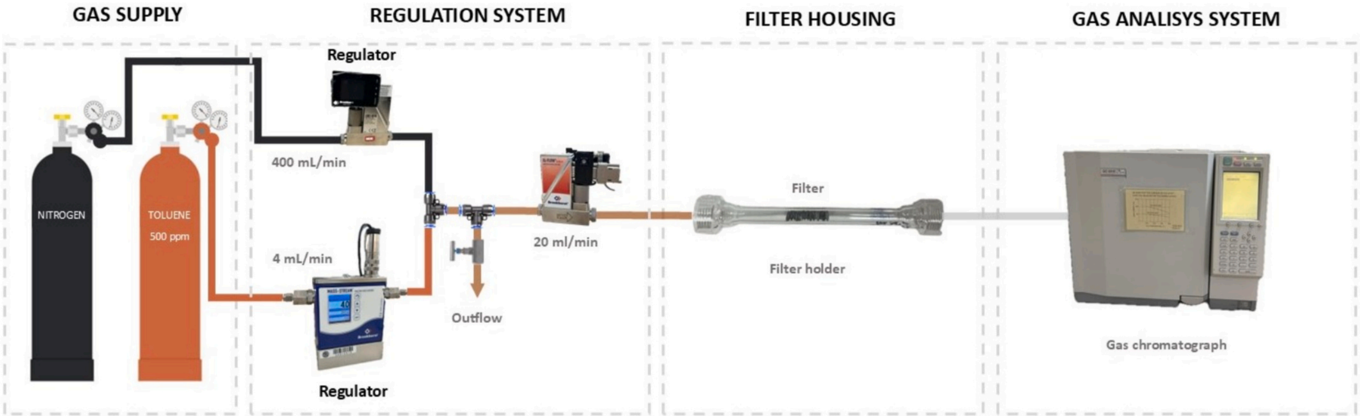

Fig. 3. Flow diagram of gas adsorption testing equipment.

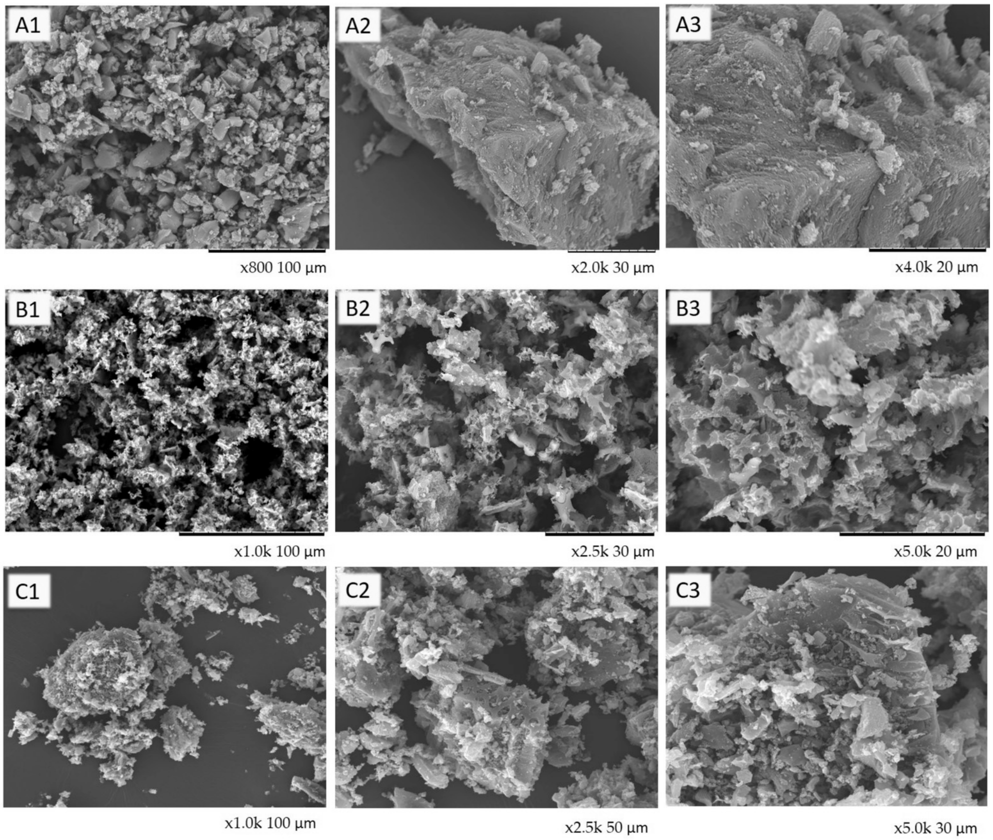

Fig. 4. SEM images of activated carbon with A) H_3PO_4: A1) 100 µm; A2) 30 µm; A3) 20 µm; B) KOH: B1) 100 µm; B2) 30 µm; B3) 20 µm, and C) Norit commercial carbon: C1) 100 µm; C2) 30 µm; C3) 20 µm.

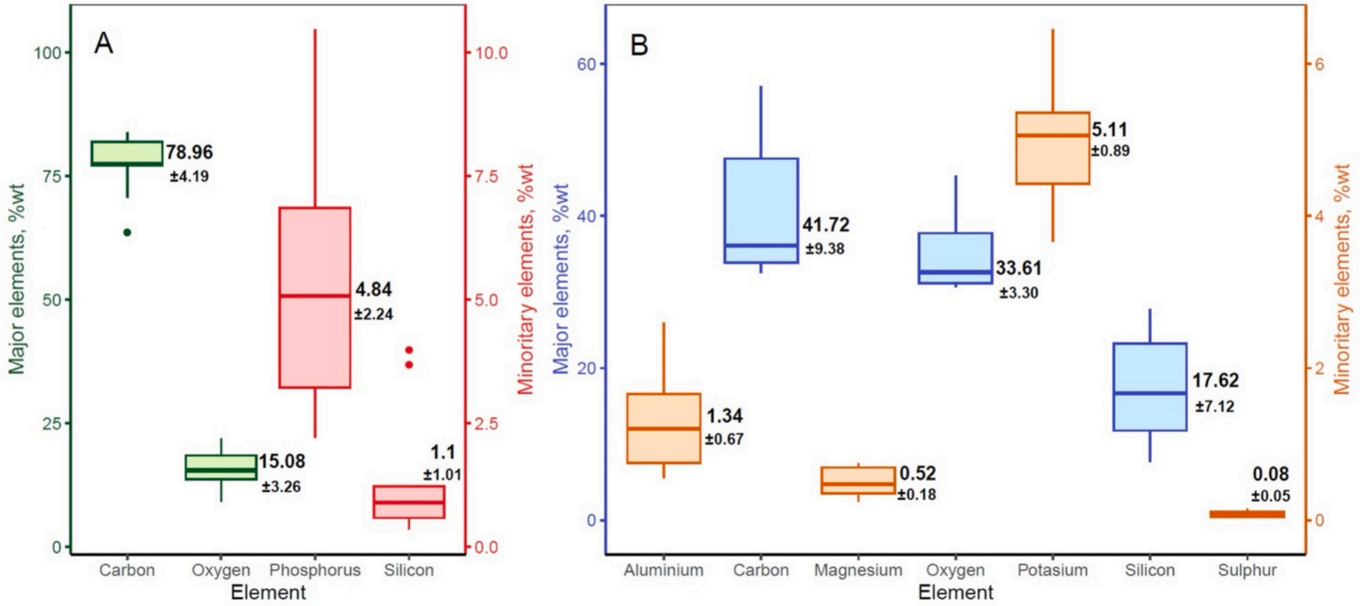

Fig. 5. EDX elemental analysis of two types of activated carbon obtained depending on the activation agent: A) H_3PO_4; B) KOH.

near 2900 cm^{-1} corresponds to C—H and possibly aliphatic C—C bonds. A prominent peak at approximately 1600 cm^{-1} suggests the presence of aromatic C═C bonds or phenolic structures. Notably, the region around 1200 cm^{-1} displays multiple signals associated with P═O, P–OH, C—O, and C–O–P bonds, confirming the incorporation of phosphorus-containing groups as a result of phosphoric acid activation. Additionally, the band near 600 cm^{-1} is indicative of C—P bonds, further supporting the presence of phosphorus functionalities. These groups are known to enhance the surface acidity and adsorption capacity of the AC, particularly for polar compounds.

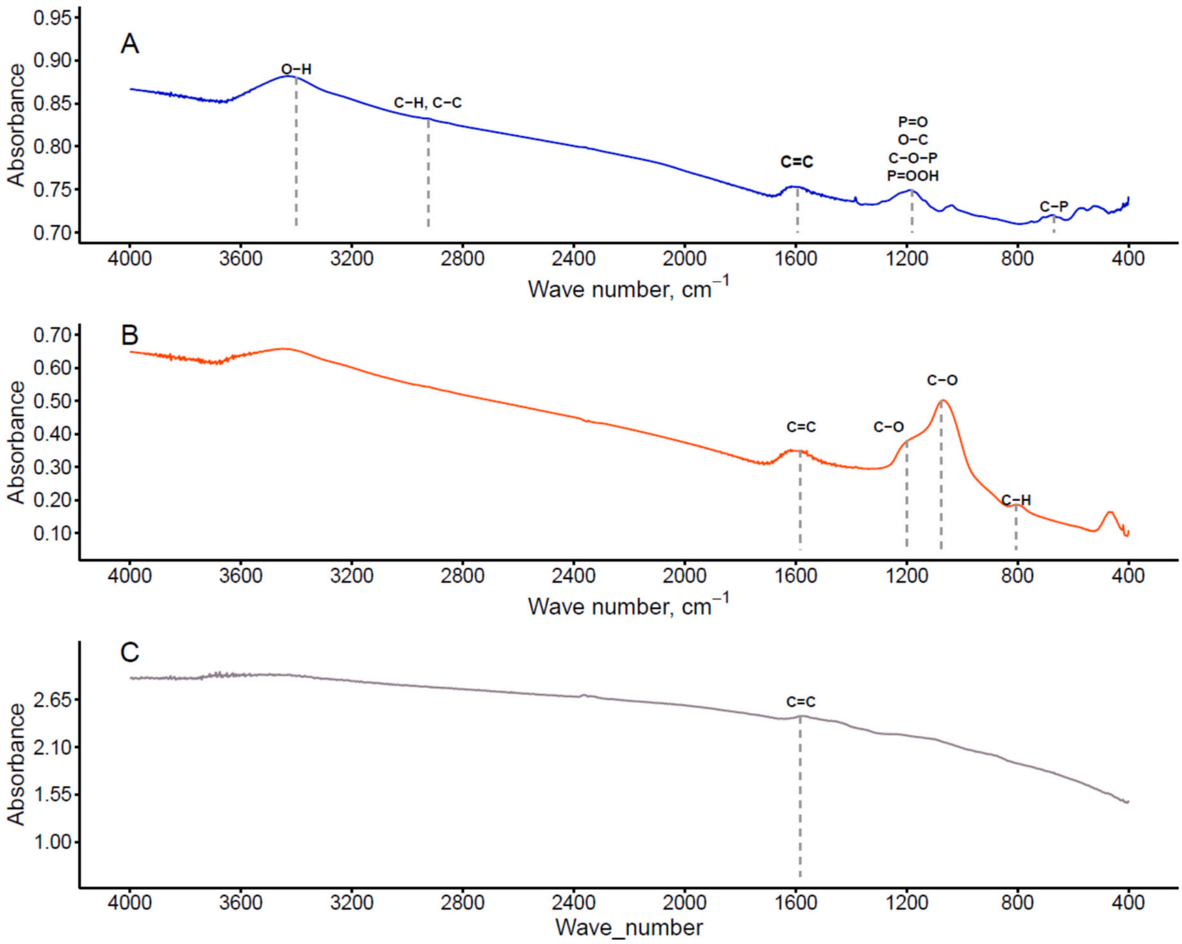

Fig. 6. FTIR spectra of A) activated carbon with H_3PO_4; B) activated carbon with KOH, and C) Norit commercial carbon.

In contrast, the FTIR spectrum of the AC treated with KOH (Fig. 6, spectrum B) reveals a simpler profile with fewer types of functional groups. The most prominent peak appears around 1600 cm^{-1}, corresponding to aromatic C═C stretching vibrations, which suggests a higher degree of graphitization. The region near 1200 cm^{-1} and below shows signals related to C—O bonds, typically found in alcohols, ethers, or phenolic structures. Additional bands between 800 and 400 cm^{-1} are attributed to out-of-plane C—H bending vibrations in substituted aromatic rings. The use of KOH, which prevents the introduction of phosphorus functionalities, promotes the development of a more aromatic and porous carbon structure with a lower degree of surface chemical functionalization. This may result in a more basic surface character and greater thermal stability, although with potentially lower affinity for polar adsorbates compared to the AC H_3PO_4.

Comparing the two activated carbons in this study with a commercial AC (Fig. 6, spectrum C), the only peak in common was observed around 1600 cm^{-1}, due to the stretching vibrations of C═O double bonds or the presence of C═C bonds. This shows that the nature of the surface functional groups depends on both the method of obtaining and activating the carbon and the nature of the raw material (Bizi, 2020; Karume et al., 2023; Malini et al., 2023).

3.1.3. *Porosity analysis*

Table 2 shows the results corresponding to the surface analysis. In both cases, the BET surface area (S_{BET}) reached values in the range of commercial carbons, with 670-fold increase in pseudostem core S_{BET} for H_3PO_4 activation and 126-fold increase for KOH activation. Comparing both carbons, the S_{BET} obtained with AC H_3PO_4 was five times greater than the S_{BET} of AC KOH. Similar results were obtained for the microporous surface (S_{MICRO}), reaching a value approximately doubled by activation with H_3PO_4. However, the S_{BET}/S_{MICRO} ratio was greater for KOH activation, with a microporous contribution of 69 %; in the case of H_3PO_4 activation, this contribution was less than 20 %. These results show that although the AC H_3PO_4 had a greater S_{BET} and S_{MICRO}, the activation process with KOH results in a carbon with a well-developed porous structure, with a significant amount of micropore in relation to the total porous area. This was confirmed with porosity values obtained. The mesoporosity of AC H_3PO_4 was 9 times greater than the mesoporosity of AC KOH; the microporosity of the AC H_3PO_4 was twice as high as that of the AC KOH. However, 32 % of the total porous surface area of the latter carbon corresponds to the micropore surface, compared to 8 % for AC H_3PO_4, which has a mainly external porous surface.

Table 2
Results of the surface analysis.

	H_3PO_4	KOH	Commercial
S_{BET} ($m^2\cdot g^{-1}$)	1531.09	287.46	592.84
S_{MICRO} ($m^2\cdot g^{-1}$)	272.04	187.17	321.65
Total porosity ($cm^3\cdot g^{-1}$)	1.84	0.249	0.515
Mesoporosity ($cm^3\cdot g^{-1}$)	1.34	0.143	0.317
Microporosity ($cm^3\cdot g^{-1}$)	0.146	0.078	0.145
Average pore diameter (nm)	4.82	3.46	3.48

The microporous surface area of AC H_3PO_4 was quite similar to that of commercial AC, as was the microporosity. On the other hand, the mesoporosity was much higher, which explains the higher S_{BET} value of this carbon. In the case of mean pore diameter, however, a greater similarity with AC KOH was obtained.

When comparing the results obtained with the porosity of other activated carbons from other types of biomass, some significant differences were observed. (Chai et al., 2024) obtained AC using three different types of biomass, carrying out alkaline activation with KOH. The S_{BET} values achieved were 1023.2 $m^2 \cdot g^{-1}$, 1234.8 $m^2 \cdot g^{-1}$ and 1081.2 $m^2 \cdot g^{-1}$ from lotus petiole, sunflower plate and lotus seedpod, respectively. These results were quite a lot higher than those obtained in the present study. The pore volume showed the same trend, being three times higher. The differences obtained could be due to the type of biomass, as well as the biomass treatment, such as the activation temperature or biomass/activator ratio. The effect of these factors can be confirmed by the study performed by (Jamil et al., 2023). In this study, wheat straw was used as raw biomass, obtaining S_{BET} equal to 529,5 $m^2 \cdot g^{-1}$ and 134.4 $m^2 \cdot g^{-1}$ with a ratio biomass/KOH of 1:3 and 1:1, respectively.

However, in the case of phosphoric acid, the results obtained in the present study were higher compared with other studies, such as the one conducted by (Xiang et al., 2025), in which activated carbon was obtained using pre-carbonized bamboo shoot shells. The S_{BET} values were equal to 681.7 $m^2 \cdot g^{-1}$ and the pore volume was 0.35 $cm^3 \cdot g^{-1}$. In the study carried out by (Zhong et al., 2024), H_3PO_4 AC also showed a S_{BET} of 389.9 $m^2 \cdot g^{-1}$ and a pore volume of 0,27 $cm^3 \cdot g^{-1}$. The carbon activation in this research was carried out using cotton stalks and at low temperature. As with the KOH activation, factors such as the type of biomass or activator concentration can significantly affect the porosity values. This is confirmed by (Xiang et al., 2025), as the effect of H_3PO_4 concentration was also studied, with an increase in adsorption capacity observed as the mass fraction of phosphoric acid increased from 30 wt% to 60 wt%.

3.2. Particle capture efficiency

Fig. 7 shows the variation in particle capture efficiency as a function of particle size for filters prepared with AC chemically treated using different activating agents: phosphoric acid (H_3PO_4) and potassium hydroxide (KOH). Filters were manufactured using two AC concentrations for each activating agent: 5 wt% and 10 wt%. The particle capture efficiency of filters without AC is also shown (w/o AC).

In all cases, a general increasing trend in capture efficiency was observed as particle size increased, which aligns with the expected behavior of filtration systems. Larger particles are more likely to be retained through mechanisms such as interception and inertial impaction, whereas smaller particles tend to escape more easily due to diffusion or their lower mass. Filters activated with H_3PO_4 exhibited consistently higher performance than those activated with KOH across the entire range of particle sizes evaluated (0.3 to 2.6 μm). For instance, in the smallest particle size range (0.3–0.374 μm), the filter treated with 10 % AC H_3PO_4 achieved a capture efficiency close to 73 %, while the one treated with 5 % AC H_3PO_4 reached approximately 55 %. In contrast, filters activated with KOH showed lower efficiencies overall, with a noteworthy exception: the 5 % AC KOH outperformed the 10 % AC KOH across all particle sizes, especially in the lower size ranges, where this difference was more pronounced.

Specifically, the 5 % AC KOH filter achieved around 26 % efficiency for 0.3–0.374 μm particles, while the 10 % AC KOH filter captured only about 22 % in the same range. This trend persisted across the particle size spectrum, suggesting that higher AC KOH concentrations do not necessarily improve performance. This behavior may indicate that, in the case of AC KOH, higher activating concentrations could lead to the formation of a less efficient porous structure, potentially due to pore collapse or over-activation effects that negatively impact the final material properties. On the other hand, for AC H_3PO_4, increasing the AC concentration consistently enhanced filter performance.

Compared to the filters without AC, all chemically treated filters generally exhibited superior particle capture efficiencies. However, in the smallest particle size range, filters activated with KOH showed a reduced retention capacity for ultrafine particles, performing slightly below the non-activated filters in this specific case. Across all treatments, efficiencies tended to converge toward high values (>90 %) starting at approximately 1.1 μm, reaching nearly 100 % for the largest particle sizes (>2 μm). Nevertheless, even within these upper size ranges, the 10 % AC H_3PO_4 filter maintained a slight performance advantage over the others, highlighting its strong retention capabilities.

The error bars shown in Fig. 8, representing the standard deviation of the data, indicate that variability was higher at the smallest particle sizes, particularly for the lower-performing filters. As particle size increased, the standard deviations generally decreased, reflecting more stable filtration behavior for larger particles, except in the filters without AC and with higher concentrations of AC KOH, which exhibited some heterogeneity in particle retention.

When analyzing the particle capture efficiency grouped by categories $PM_{0.3}$, PM_1, and $PM_{2.5}$ (PM_{10} results are practically identical to $PM_{2.5}$ due to the minimal amount of large particles generated by the test

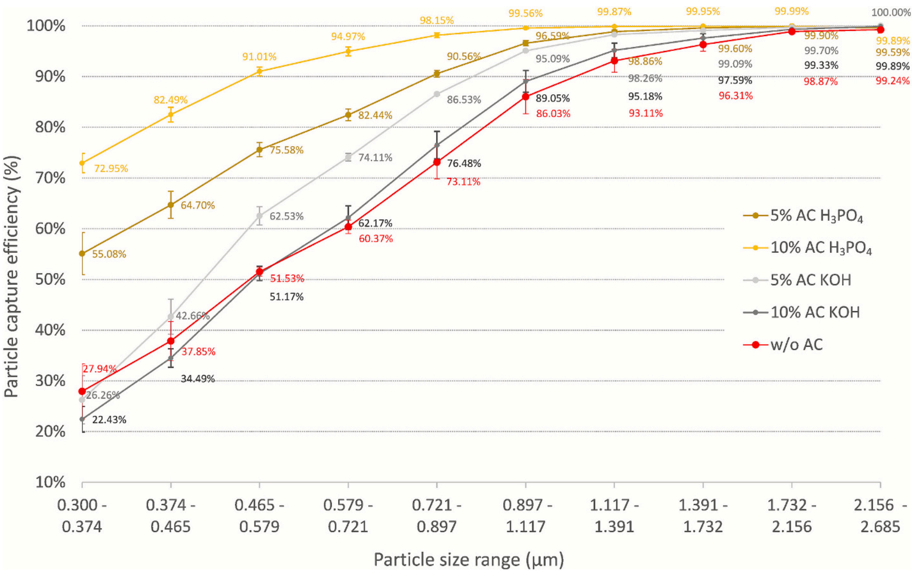

Fig. 7. Particle capture efficiency (mean values and standard deviation) of activated carbon filters.

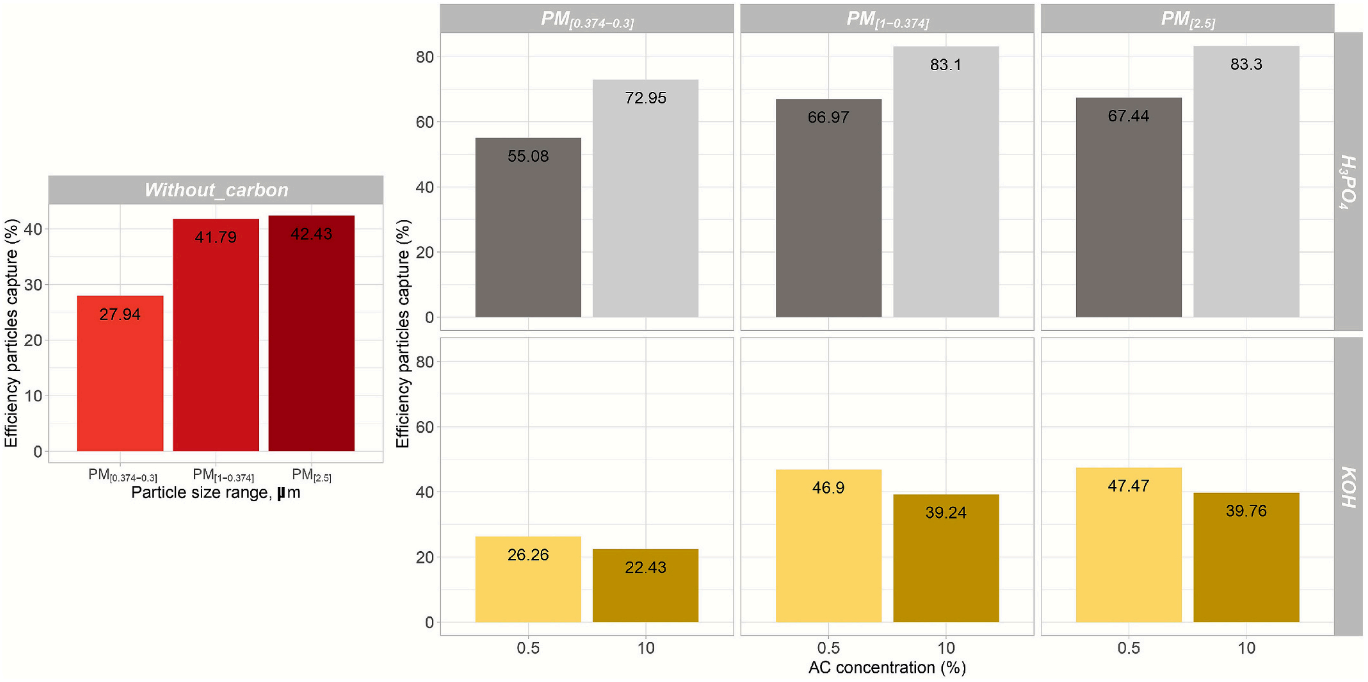

Fig. 8. Capture efficiency for different PM size groups (mean values and standard deviation).

equipment), a similar pattern appears regarding the performance of AC KOH filters compared to non-activated filters (Fig. 8). For the ultrafine particle group ($PM_{0.3}$), the filters treated with KOH at both 5 % and 10 % AC concentrations exhibited lower capture efficiencies than the filter without AC. Specifically, the non-activated filter achieved an efficiency of 27.94 %, while the 5 % AC KOH and 10 % AC KOH filters reached only 26.26 % and 22.43 %, respectively. This confirms that, in this particle size group, KOH activation may negatively affect the filter's ability to retain ultrafine particles, potentially due to surface chemistry alterations that reduce adsorption affinity at the nanoscale.

In contrast, for the PM_1 group, the 5 % AC KOH filter outperformed the non-activated filter, achieving 46.98 % efficiency compared to 41.79 %. However, the 10 % AC KOH filter again underperformed, with a capture efficiency of 39.24 %, slightly below the non-activated filter. A similar trend was observed in the $PM_{2.5}$ group, where the 5 % AC KOH filter maintained the highest efficiency (47.47 %), followed by the non-activated filter (42.43 %) and the 10 % AC KOH filter (39.76 %). These results confirm that a moderate concentration of AC KOH (5 %) can enhance filtration performance for fine and coarse particles, but higher concentrations (10 %) may compromise structural integrity or lead to suboptimal pore distribution, reducing overall effectiveness.

In the case of filters activated with H_3PO_4, the particle capture efficiency grouped by PM categories reveals a consistent and pronounced improvement over non-activated filters. The data show that H_3PO_4 activation significantly enhances filtration performance across all particle size groups, with a clear positive correlation between AC concentration and efficiency. For the ultrafine particle group ($PM_{0.3}$), the filter without AC achieved a capture efficiency of 27.94 %, while the 5 % AC H_3PO_4 filter reached 55.08 % (about twice as high), and the 10 % AC H_3PO_4 filter achieved 72.95 % (2.6 times higher). This trend continues in the PM_1 group, where the non-activated filter captured 41.79 % of particles, compared to 66.97 % (1.6 times higher) for the 5 % AC H_3PO_4 filter and 83.10 % (about twice as high) for the 10 % AC H_3PO_4 filter. For the $PM_{2.5}$ group, the performance remains consistent with the previous trends. The non-activated filter reached 42.43 % efficiency, while the 5 % AC H_3PO_4 and 10 % AC H_3PO_4 filters achieved 67.44 % (1.60 times higher) and 83.30 % (1.96 times higher), respectively.

Unlike the behavior observed with AC KOH filters, where higher concentrations did not consistently improve performance and even led to reduced efficiency in some PM groups, the AC H_3PO_4 filters demonstrated a clear and proportional improvement with increasing activation level. This contrast highlights the superior suitability of phosphoric acid as a chemical activator for applications requiring high-efficiency filtration, particularly in environments where ultrafine and fine particle control is critical. The consistent performance across PM groups and the absence of efficiency reversal at higher activation levels underscore the robustness of H_3PO_4 activation in enhancing the functional properties of the filter media.

To confirm whether the differences observed in particle capture efficiencies were statistically significant, a multivariate mean contrast was carried out, using the activator type as criterion for creating two independent samples. Since each sample showed a normal distribution according to the results of Shapiro-Wilks test (*p*-values >0.05), the two-samples Hotelling's T2 test was applied, considering the particles size range ($PM_{0.3}$, PM_1, and $PM_{2.5}$) and activator concentration (0, 5 and 10 %) as study variables. A significant difference was observed between the average capture efficiency in AC KOH filters and average capture efficiency in AC H_3PO_4 filters, as the F statistic showed a value well above 1, with a p-value well below 0.05 (Table 3).

Considering the results obtained in the previous test, each sample was analyzed separately, studying the effect of the activator concentration. To do this, the Kruskal-Wallis test was applied, due to the lower number of data (Table 4). The results obtained in this test showed that in the filters to which AC KOH was added, no significant differences were observed with respect to activator concentration. These results were confirmed with Dunn's pairwise test. However, in the case of filters manufactured with AC H_3PO_4 activated carbon, significant differences

Table 3
Results of Shapiro-Wilk's test and two-sample Hotelling's T2 test.

		AC KOH	AC H_3PO_4
Shapiro-Wilk's test	p-value	0.09	0.07
Hotelling's T2 test	T2 statistic	29.9	
	F statistic	29.9	
	p-value	$1.31 \cdot 10^{-6}$	
	Mean sample (%)	37.7	60.7

Table 4

p-values for the Kruskal-Wallis test and Dunn's test considering particle size range and activator concentrations.

	AC KOH			AC H_3PO_4		
	Kruskal-Wallis test	Dunn test		Kruskal-Wallis test	Dunn test	
$PM_{0.3}$	0.39	0–10	0.53	0.03	0–10	0.02*
		0–5	1		0–5	0.54
		5–10	1		5–10	0.54
PM_1	0.20	0–10	1	0.03	0–10	0.02*
		0–5	1		0–5	0.54
		5–10	0.221		5–10	0.54
$PM_{2.5}$	0.20	0–10	1	0.03	0–10	0.02*
		0–5	1		0–5	0.54
		5–10	0.221		5–10	0.54

[*] 95 % statistical significance

were observed between a 10 % addition and no addition of activated carbon, obtaining a p-value lower than 0.05 in both tests.

To ensure the results reflect real-world air quality impacts, the ISO 16890 weighting method was applied. For PM_{10}, the weighting was distributed as follows: 10 % for particles between 0.3 and 0.5 µm, 30 % for particles between 0.5 and 1 µm, 30 % for particles between 1 and 2.5 µm, and 30 % for particles between 2.5 and 10 µm. For $PM_{2.5}$, the weighting was 10 % for particles between 0.3 and 0.5 µm, 25 % for particles between 0.5 and 1 µm, and 60 % for particles between 1 and 2.5 µm. These weightings were used to calculate the weighted average capture efficiency for each treatment and are shown in Fig. 9.

For $PM_{2.5}$, the untreated filter achieved a capture efficiency of 78.02 %, while the highest-performing treatment, 10 % AC H_3PO_4, reached 92.16 %. Similarly, for PM_{10}, the untreated filter captured 82.54 % of particles, whereas the 10 % AC H_3PO_4 treatment achieved a capture efficiency of 96.03 %. Other treatments also showed notable improvements, particularly the 5 % AC KOH and 5 % AC H_3PO_4 filters, which consistently outperformed the untreated baseline. The application of ISO 16890 weighting ensures that the reported efficiencies are representative of real-world conditions, providing a reliable basis for comparing filter treatments in terms of their health-relevant performance. Due to the weighting factors, which assign higher weight to lower efficiencies in the case of PM10, the weighted capture efficiencies of 5 % AC KOH and 10 % AC KOH for PM2.5 are slightly higher than for PM10.

3.3. Pressure drop behavior

Table 5 presents the pressure drop (Pa) measured across filter media modified with different activating agents. The unmodified control (w/o AC) exhibited the lowest pressure drop (261.67 Pa), serving as the baseline. Upon activation, all samples experienced increased resistance to airflow, with the extent varying depending on the activation agent and concentration. Filters activated with KOH exhibited moderate pressure drops: 675.00 Pa (5 %) and 478.33 Pa (10 %), while those treated with H_3PO_4 showed higher values; 514.33 Pa (5 %) and a maximum of 804.33 Pa (10 %). Despite AC KOH samples having lower specific surface areas (287.46 $m^2 \cdot g^{-1}$) and total porosity (0.249 $cm^3 \cdot g^{-1}$) compared to AC H_3PO_4 samples (1531.09 $m^2 \cdot g^{-1}$, 1.84 $cm^3 \cdot g^{-1}$, respectively), they offered lower airflow resistance. This suggests that KOH activation produces a more open or permeable pore network, despite lower porosity metrics.

The AC H_3PO_4 samples, although possessing significantly higher surface area and mesoporosity (1.34 $cm^3 \cdot g^{-1}$), also had a higher pressure drop, especially at 10 %, possibly due to increased tortuosity and greater internal pore volume that impedes airflow. This increase in airflow resistance has important practical implications, as it is directly associated with higher energy consumption during operation. In particular, the maximum pressure drop measured for the 10 % AC H_3PO_4 sample (804.33 Pa) may lead to increased fan power requirements compared to AC KOH or unmodified filters. Additionally, the average pore diameter was larger for AC H_3PO_4 samples (4.82 nm) compared to KOH (3.46 nm), which may contribute to greater gas adsorption capacity but not necessarily better permeability. Overall, the results highlight a trade-off between surface area development and airflow resistance in chemically activated carbon materials, where H_3PO_4 yields highly porous structures beneficial for adsorption or particle capture, but at the cost of higher pressure drop.

To carry out the statistical study of pressure drops, the Kruskal-Wallis

Table 5

Pressure drop of filters tested.

Filter type	Mean pressure drop (Pa)	Standard deviation (Pa)
w/o AC	261.67	4.71
5 % AC KOH	675.00	16.51
10 % AC KOH	478.33	9.43
5 % AC H_3P0_4	514.33	15.52
10 % AC H_3P0_4	804.33	35.37

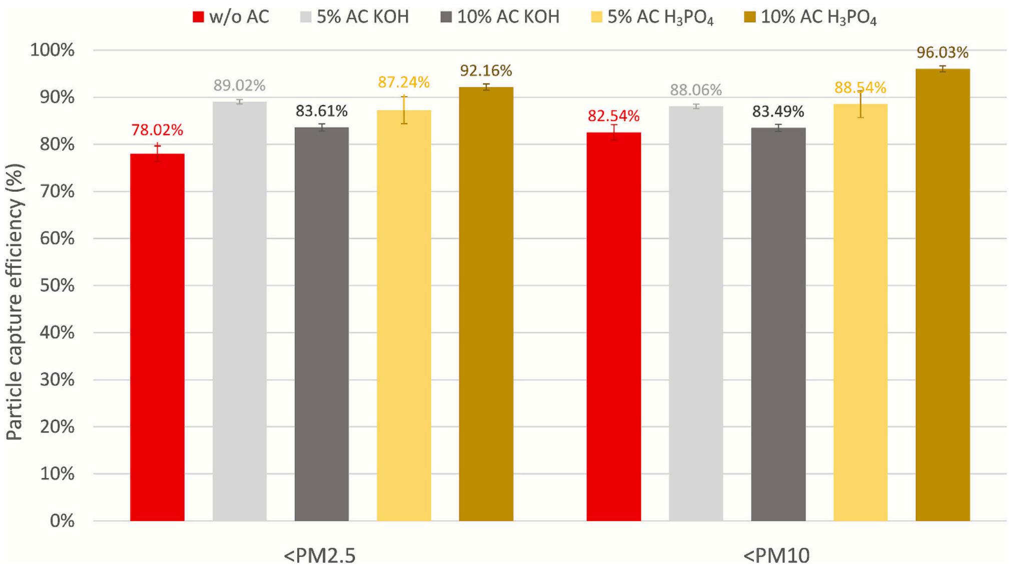

Fig. 9. Weighted capture efficiency for different PM size groups (mean values and standard deviation).

test was applied due to the small sample size, considering the type and concentration of the activator as a factorial variable. The results showed significant differences, with a *p*-value well below 0.05. Next, the Dunn's test was applied as a post-hoc analysis, obtaining the results shown in Table 6.

In any case, these pressure drops (ranging from 478 to 804.33 Pa) are consistent with those reported for commercial HEPA and ULPA filters, which typically exhibit 250–450 Pa for H13–H14 and up to 600 Pa for U15–U17 at nominal airflow, according to EN 1822/ISO 29463. These results indicate that, despite the slightly higher ΔP, the developed filters maintain airflow within acceptable operational limits while providing enhanced particle capture efficiency. Accordingly, future optimization efforts should prioritize minimizing airflow resistance by fine-tuning activation conditions, optimizing pore architecture, and adjusting filter media thickness, while preserving the high filtration efficiency achieved by AC H_3PO_4 materials.

3.4. Gas capture efficiency

Fig. 10 presents the toluene breakthrough curves for the different filters, expressed as the percentage of unadsorbed toluene (%) over time. The horizontal purple line (100 %) represents the inlet of toluene in the gas stream, serving as the saturation limit when no adsorption occurs. Since this analysis was carried out by stacking 14 units of mini filter discs to ensure adequate gas adsorption resolution, only the filters with a 5 % AC concentration were used.

The sample without activated carbon (w/o AC) displays the poorest performance. Toluene begins to break through within the first 20 min, and full saturation is reached before 130 min. This behavior reflects a very limited adsorption capacity, confirming the critical role of AC in retaining volatile organic compounds (VOCs). The material activated with H_3PO_4 performs slightly better. Breakthrough begins around 25 min, and saturation occurs before 250 min. The sharp rise in unadsorbed toluene suggests a fast consumption of available adsorption sites, likely due to its pore structure, which—despite having a high surface area (1531.09 $m^2 \cdot g^{-1}$)—may have limited pore accessibility or lower affinity for toluene molecules under dynamic flow conditions.

The commercial filter exhibits significantly improved performance, delaying breakthrough until approximately 100 min, with a gradual increase in unadsorbed toluene over time. Saturation is reached around 300 min. This indicates a moderate adsorption capacity and kinetic profile, typical of commercial-grade AC. Notably, the material activated with KOH exhibits superior toluene adsorption performance. It maintains near-zero unadsorbed toluene levels for up to 75 min, with a gentle slope indicating a slower approach to saturation. Even after 350 min, the curve remains below the inlet concentration, suggesting residual adsorption capacity. Despite the higher specific surface area and total porosity observed for the AC prepared with H_3PO_4 (1531.09 $m^2 \cdot g^{-1}$ and 1.84 $cm^3 \cdot g^{-1}$, respectively), the KOH-treated AC exhibits superior toluene adsorption performance. This behavior can be attributed primarily to differences in surface chemistry and pore structure: KOH activation typically results in a more hydrophobic and basic surface, enhancing interactions with non-polar molecules such as toluene, and narrower average pore diameter (3.46 nm for KOH versus 4.82 nm for H_3PO_4) improve confinement and accessibility. In addition, the higher mineral/ash content detected in KOH-activated samples may contribute to adsorption, potentially acting as a molecular sieve or providing silica-like adsorption sites. However, further studies are required to isolate and quantify the contribution of mineral/ash components to the adsorption performance. These findings highlight that adsorption capacity is not solely dependent on textural properties such as surface area or total porosity (Nateq et al., 2025; Yaghoot-Nezhad et al., 2020), but is also significantly influenced by pore size distribution and surface functional groups.

Table 6
Results of Dunn's test. “ns” means no significance.

Paired-sample	p-Value	Statistical significance
AC H_3PO_4 (10 %) – w/o AC	1	ns
AC H_3PO_4 (5 %) – w/o AC	0.13	ns
AC H_3PO_4 (10 %) – AC H_3PO_4 (5 %)	0.99	ns
AC KOH (10 %) – w/o AC	0.01	99 %
AC KOH (5 %) – w/o AC	0.99	ns
AC KOH (10 %) – A CKOH (5 %)	0.99	ns
AC H_3PO_4 (10 %) – AC KOH (10 %)	0.13	ns
AC H_3PO_4 (5 %) – AC KOH (10 %)	1	ns
AC H_3PO_4 (10 %) – AC KOH (5 %)	1	ns
AC H_3PO_4 (5 %) – AC KOH (5 %)	1	ns

Although the adsorption results presented here focus on toluene as a model VOC, the filter's porous structure and surface chemistry suggest that it may also effectively adsorb other aromatic compounds. Previous studies with mesoporous graphene and activated carbon show similar adsorption efficiencies for toluene, xylene, and benzene, often exceeding 90 %, due to π–π interactions with the aromatic rings (Lim et al., 2019; Mobasser et al., 2022). While toluene tests are widely accepted as indicative of performance for chemically similar VOCs, further studies are needed to confirm adsorption capacities for polar or structurally distinct compounds.

4. Conclusion

In this study, the particle filtration and toluene adsorption capacities of freeze-dried filters derived from banana cultivation biomass (used both as the structural matrix and as the source of activated carbon) were evaluated, enabling a dual valorization of the raw material for environmental filtration applications.

The incorporation of activated carbon significantly enhanced particulate matter filtration efficiency across nearly all particle sizes analyzed (0.3 to 10 μm), with particularly strong performance observed for AC H_3PO_4, which achieved 95 % efficiency for particles ≥0.5 μm. This improvement is attributed to its higher surface area and internal porosity, promoting enhanced particle retention compared to AC KOH. In the case of toluene adsorption, however, AC KOH —despite its lower porosity — demonstrated superior performance due to its surface functional groups, which showed greater affinity for non-polar compounds such as toluene. Its adsorption capacity exceeded that of both AC H_3PO_4 and commercial reference filters.

These findings highlight distinct application potentials for each type of activated carbon: AC H_3PO_4 is more suitable for fine particle filtration, while AC KOH excels in VOC adsorption. Given the complementary strengths of both materials, a composite or layered filter design emerges as an optimal strategy. By combining AC KOH and AC H_3PO_4 layers — or integrating both within a single filter substrate — it is possible to balance low airflow resistance with high filtration and adsorption efficiency, achieving multifunctional performance in a single device. Moreover, the use of banana crop biomass as both a structural base and a carbon precursor offers a sustainable and biodegradable alternative for air pollution control, reducing dependence on synthetic and non-biodegradable materials. Despite these promising results, further research is needed to address additional production aspects of multifunctional filters. Key priorities include evaluating overall manufacturing costs, optimizing process energy demands, characterizing particulate saturation curves, mechanical strength, long-term durability, certifying biodegradability, and conducting a comprehensive environmental life-cycle assessment. Importantly, the negligible cost and wide availability of the raw material, combined with the use of established industrial technologies such as freeze-drying and carbonization, represent strong enablers for potential commercial development.

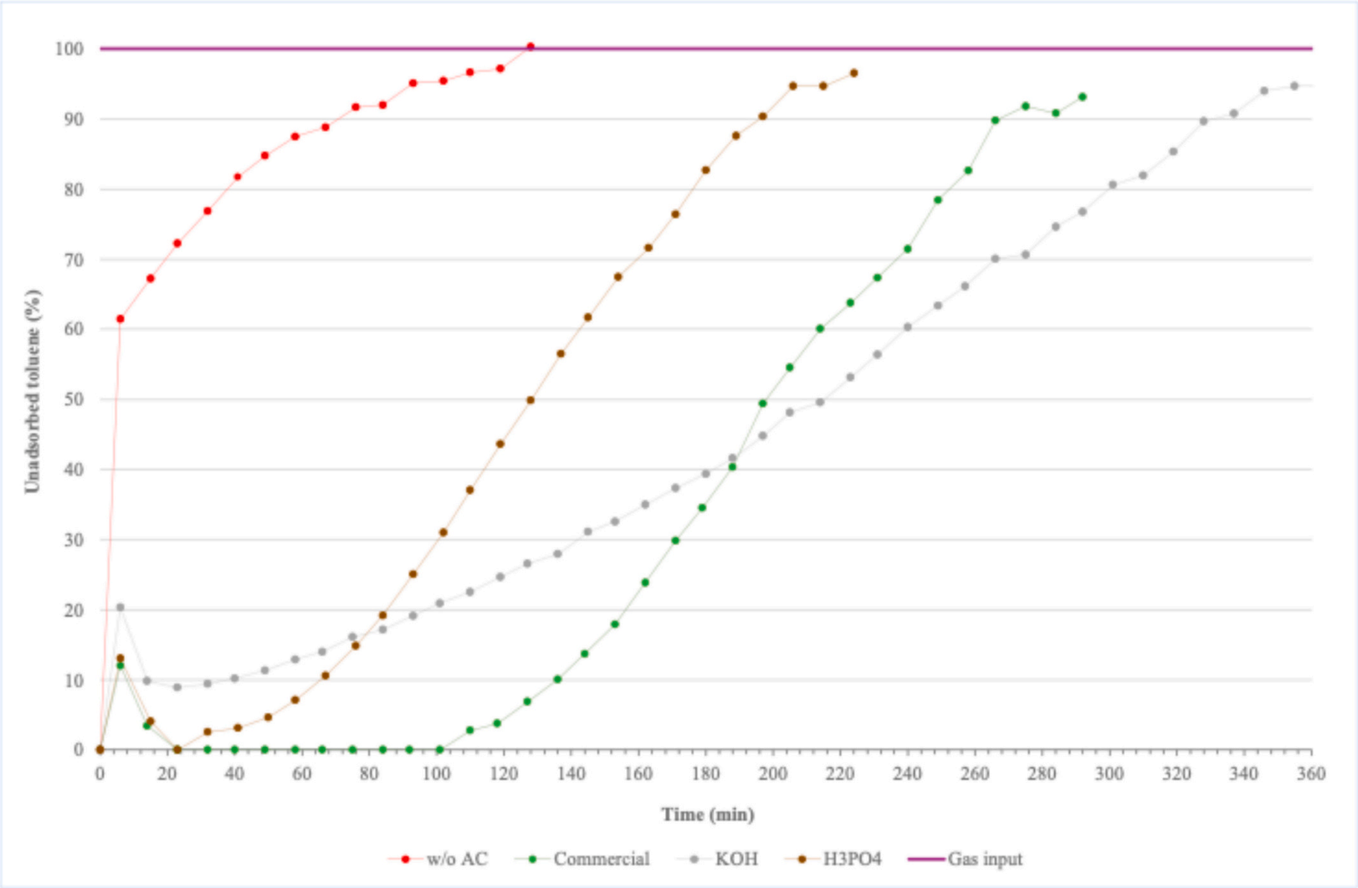

Fig. 10. Unadsorbed toluene tests.

CRediT authorship contribution statement

Yumara Martín-Cruz: Validation, Software, Methodology, Investigation, Writing – review & editing, Writing – original draft. **Pablo Bordón:** Validation, Supervision, Software, Methodology, Investigation, Conceptualization, Writing – review & editing, Writing – original draft. **Teresa Saura-Cayuela:** Investigation. **Mario Monzón:** Methodology, Conceptualization, Writing – review & editing, Writing – original draft. **Elisenda Pulido-Melián:** Validation, Supervision, Software, Methodology, Investigation, Funding acquisition, Formal analysis, Conceptualization, Writing – review & editing, Writing – original draft.

Declaration of competing interest

The authors declare that they have no known competing financial interests or personal relationships that could have appeared to influence the work reported in this paper.

Acknowledgment

This research was funded by Fundación CajaCanarias and Fundación Bancaria ‘la Caixa’ as part of the FILTRACEL project (code: 2021ECO2).

Appendix A. Supplementary data

Supplementary data to this article can be found online at https://doi.org/10.1016/j.biteb.2025.102531.

Data availability

Data will be made available on request.

References

Adami, G., Cattani, G., Rossini, M., Viapiana, O., Olivi, P., Orsolini, G., Bertoldo, E., Fracassi, E., Gatti, D., Fassio, A., 2022. Association between exposure to fine particulate matter and osteoporosis: a population-based cohort study. Osteoporos. Int. 33, 169–176. https://doi.org/10.1007/s00198-021-06060-9.

Arias-Pérez, R.D., Taborda, N.A., Gómez, D.M., Narvaez, J.F., Porras, J., Hernandez, J.C., 2020. Inflammatory effects of particulate matter air pollution. Environ. Sci. Pollut. Res. 27, 42390–42404. https://doi.org/10.1007/s11356-020-10574-w.

Asprocan, 2024. Estadísticas 2023 de Producción y Comercialización del Plátano de Canarias IGP [WWW Document]. URL. https://platanodecanarias.es/wp-content/uploads/2024/05/PdC_Anuario-Estadistico_23.pdf (accessed 9.13.25).

Atalie, D., Chen, Z.-X., Li, H., Liang, C.-G., Gao, M.-C., Cheng, X.-X., Ma, P.-C., 2024. Eco-friendly and highly efficient PM0.3 air filter made from nonwoven basalt fiber and electrospun nanocellulose fiber. J. Hazard. Mater. 478, 135608. https://doi.org/10.1016/j.jhazmat.2024.135608.

Bizi, M., 2020. Sulfamethoxazole Removal from Drinking Water by Activated Carbon: Kinetics and Diffusion Process. Molecules 25, 4656. https://doi.org/10.3390/molecules25204656.

Buyukada-Kesici, E., Gezmis-Yavuz, E., Aydin, D., Cansoy, C.E., Alp, K., Koseoglu-Imer, D.Y., 2021. Design and fabrication of nano-engineered electrospun filter media with cellulose nanocrystal for toluene adsorption from indoor air. Mater. Sci. Eng. B 264, 114953. https://doi.org/10.1016/j.mseb.2020.114953.

Cai, Y., Yang, Q., Wang, E., Liang, Y., Han, W., Miao, Y., Huang, J., Zhang, W., 2024. Developing cellulose nanofibrils/Na-montmorillonite composite air filter with efficient filtration ability for PM2.5 and adsorption of formaldehyde. Appl. Surf. Sci. 657, 159737. https://doi.org/10.1016/j.apsusc.2024.159737.

Chai, W., Wang, F., Miao, Z., Che, N., 2024. Hydrophilic porous activated biochar with high specific surface area for efficient capacitive deionization. Desal. Water Treat. 320, 100617. https://doi.org/10.1016/j.dwt.2024.100617.

Chew, S., Kolosowska, N., Saveleva, L., Malm, T., Kanninen, K.M., 2020. Impairment of mitochondrial function by particulate matter: Implications for the brain. Neurochem. Int. 135, 104694. https://doi.org/10.1016/j.neuint.2020.104694.

Chew, T.W., H`Ng, P.S., Luqman Chuah Abdullah, B.C.T.G., Chin, K.L., Lee, C.L., Mohd Nor Hafizuddin, B.M.S., TaungMai, L., 2023. A Review of Bio-based Activated Carbon Properties Produced from Different Activating Chemicals during Chemicals Activation Process on Biomass and its potential for Malaysia. Materials 16, 7365. https://doi.org/10.3390/ma16237365.

Cordeiro, J.L.C., Menezes, R.S.G., da Silva, M.C.M., dos Santos, M.B., Cruz, F.T., Andrade, H.M.C., Mascarenhas, A.J.S., Fiuza-Junior, R.A., 2024. High removal of volatile organic compounds on hierarchical carbons prepared from agro-industrial waste of banana fruit production for air decontamination. Environ. Sci. Pollut. Res. 31, 62730–62744. https://doi.org/10.1007/s11356-024-35394-0.

Cui, B., Ding, J., Xie, H., Ji, T., Yang, C., Cui, Y., Shu, X., Dai, W., Wang, W., Li, S., 2025. Processing wheat straw into strong and flexible cellulose fiber bundle: Waste-to-wealth strategy. Int. J. Biol. Macromol. 314, 144382. https://doi.org/10.1016/j.ijbiomac.2025.144382.

Fallah, A., Ghiassi Tarzi, B., Asadi, G., Farhoodi, M., 2024. Fabrication of reusable 3D hierarchically porous air filtration based on multifunctional nanoclay-embedded cellulose electrospun nanofiber. Int. J. Biol. Macromol. 279, 135391. https://doi.org/10.1016/j.ijbiomac.2024.135391.

Fuqua, M.A., Huo, S., Ulven, C.A., 2012. Natural Fiber Reinforced Composites. Polym. Rev. 52, 259–320. https://doi.org/10.1080/15583724.2012.705409.

Gough, C.R., Callaway, K., Spencer, E., Leisy, K., Jiang, G., Yang, S., Hu, X., 2021. Biopolymer-based Filtration Materials. ACS. Omega 6, 11804–11812. https://doi.org/10.1021/acsomega.1c00791.

Herzog, W., Parameswaran, L., Tysk, S., Robinson, P., 2022. Filtration Efficiency Test Report. Massachusetts.

Hu, Q., Gao, X., Zhang, H., Si, T., Tang, X., Peng, L., 2023. High-speed shear-induced micro regenerated cellulose materials preparation: a promising solution for highly efficient and low pressure drop air filtration using agricultural waste. Chem. Eng. J. 476, 146603. https://doi.org/10.1016/j.cej.2023.146603.

Ioannidou, O., Zabaniotou, A., 2007. Agricultural residues as precursors for activated carbon production—a review. Renew. Sust. Energ. Rev. 11, 1966–2005. https://doi.org/10.1016/j.rser.2006.03.013.

Jamil, U., Zeeshan, M., Khan, S.R., Saeed, S., 2023. Synthesis and two-step KOH based activation of porous biochar of wheat straw and waste tire for adsorptive exclusion of chromium (VI) from aqueous solution; thermodynamic and regeneration study. J. Water Process Eng. 53, 103892. https://doi.org/10.1016/j.jwpe.2023.103892.

Jawaid, M., Abdul Khalil, H.P.S., 2011. Cellulosic/synthetic fibre reinforced polymer hybrid composites: a review. Carbohydr. Polym. https://doi.org/10.1016/j.carbpol.2011.04.043.

Kakom, S.M., Abdelmonem, N.M., Ismail, I.M., Refaat, A.A., 2024. Correction: Activated Carbon from Sugarcane Bagasse Pyrolysis for Heavy Metals Adsorption. Sugar Tech. 26, 312. https://doi.org/10.1007/s12355-023-01335-3.

Kanagasabai, T., Xie, W., Yan, L., Zhao, L., Carter, E., Guo, D., Daskalopoulou, S.S., Chan, Q., Elliott, P., Ezzati, M., Yang, X., Xie, G., Kelly, F., Wu, Y., Baumgartner, J., 2022. Household Air Pollution and Blood pressure, Vascular damage, and Subclinical Indicators of Cardiovascular Disease in older Chinese adults. Am. J. Hypertens. 35, 121–131. https://doi.org/10.1093/ajh/hpab141.

Karume, I., Bbumba, S., Tewolde, S., Mukasa, I.Z.T., Ntale, M., 2023. Impact of carbonization conditions and adsorbate nature on the performance of activated carbon in water treatment. BMC Chem. 17, 162. https://doi.org/10.1186/s13065-023-01091-1.

Kundu, S., Khandaker, T., Anik, M.A.-A.M., Hasan, Md.K., Dhar, P.K., Dutta, S.K., Latif, M.A., Hossain, M.S., 2024. A comprehensive review of enhanced CO 2 capture using activated carbon derived from biomass feedstock. RSC Adv. 14, 29693–29736. https://doi.org/10.1039/D4RA04537H.

Li, X., Zhang, L., Yang, Z., Wang, P., Yan, Y., Ran, J., 2020. Adsorption materials for volatile organic compounds (VOCs) and the key factors for VOCs adsorption process: a review. Sep. Purif. Technol. 235, 116213. https://doi.org/10.1016/j.seppur.2019.116213.

Lim, S.T., Kim, J.H., Lee, C.Y., Koo, S., Jerng, D.-W., Wongwises, S., Ahn, H.S., 2019. Mesoporous graphene adsorbents for the removal of toluene and xylene at various concentrations and its reusability. Sci. Rep. 9, 10922. https://doi.org/10.1038/s41598-019-47100-z.

Lin, P., Xia, Y., Liu, Z., 2022. Influence of different activators on the structure and properties of activated carbon based on bamboo fiber. Polymers (Basel) 14, 5500. https://doi.org/10.3390/polym14245500.

Malini, K., Selvakumar, D., Kumar, N.S., 2023. Activated carbon from biomass: Preparation, factors improving basicity and surface properties for enhanced CO2 capture capacity – a review. J. CO_2 Util. 67, 102318. https://doi.org/10.1016/j.jcou.2022.102318.

Mannan, M., Al-Ghamdi, S.G., 2021. Indoor Air Quality in buildings: a Comprehensive Review on the Factors Influencing Air Pollution in Residential and Commercial Structure. Int. J. Environ. Res. Public Health 18, 3276. https://doi.org/10.3390/ijerph18063276.

Martín-Cruz, Y., Bordón, P., Pulido-Melián, E., Saura-Cayuela, T., Monzón, M., 2024. Development of cellulose air filters for capturing fine and ultrafine particles through the valorization of banana cultivation biomass waste. Environments - MDPI 11. https://doi.org/10.3390/environments11030050.

Mata, T.M., Martins, A.A., Calheiros, C.S.C., Villanueva, F., Alonso-Cuevilla, N.P., Gabriel, M.F., Silva, G.V., 2022. Indoor Air Quality: a Review of cleaning Technologies. Environments 9, 118. https://doi.org/10.3390/environments9090118.

Mobasser, S., Wager, Y., Dittrich, T.M., 2022. Indoor Air Purification of Volatile Organic Compounds (VOCs) using activated carbon, zeolite, and organosilica sorbents. Ind. Eng. Chem. Res. 61, 6791–6801. https://doi.org/10.1021/acs.iecr.1c04732.

Monzón, M.D., 2014. Method and machine for obtaining fibre from leaves. WO 2014/174115.

Mostazo-López, M.J., Salinas-Torres, D., Ruiz-Rosas, R., Morallón, E., Cazorla-Amorós, D., 2019. Nitrogen-doped superporous activated carbons as electrocatalysts for the oxygen reduction reaction. Materials 12. https://doi.org/10.3390/ma12081346.

Nateq, K., Shohani Zadeh, M., Amarzadeh, M., Rostami, M., Danaee, I., Khosravi-Nikou, M.R., 2025. In situ construction of green ZnFe2O4/sub-5nm N, Cu dual-doped SnO2 S-scheme heterostructure with the boosted spatial charge separation towards decontamination of tetracycline: Mechanistic perspectives and aquatic hazard assessment. J. Environ. Manag. 389. https://doi.org/10.1016/j.jenvman.2025.126135.

Neme, I., Gonfa, G., Masi, C., 2022. Activated carbon from biomass precursors using phosphoric acid: a review. Heliyon. https://doi.org/10.1016/j.heliyon.2022.e11940.

Nie, J., Sun, B., Jiao, T., Liao, J., Zhang, M., Yang, R., Li, Y., 2025. Biodegradable air filter with electrospun composite nanofibers and cellulose fibers dual network: Enhanced electrostatic adsorption, humidity resistance, and extended service life. J. Hazard. Mater. 489, 137557. https://doi.org/10.1016/j.jhazmat.2025.137557.

NSW Government, 2025. Common Air Pollutants and their Health Effects [WWW Document]. URL. https://www.health.nsw.gov.au/environment/air/Pages/common-air-pollutants.aspx.

Pang, L., Yu, W., Lv, J., Dou, Y., Zhao, H., Li, S., Guo, Y., Chen, G., Cui, L., Hu, J., Zhao, Y., Zhao, Q., Chen, Z.-J., 2023. Air pollution exposure and ovarian reserve impairment in Shandong province, China: the effects of particulate matter size and exposure window. Environ. Res. 218, 115056. https://doi.org/10.1016/j.envres.2022.115056.

Park, T.H., Park, S., Cho, M.K., Kim, S., 2022. Associations of particulate matter with atopic dermatitis and chronic inflammatory skin diseases in South Korea. Clin. Exp. Dermatol. 47, 325–334. https://doi.org/10.1111/ced.14910.

Radbel, J., Rebuli, M.E., Kipen, H., Brigham, E., 2024. Indoor air pollution and airway health. J. Allergy Clin. Immunol. 154, 835–846. https://doi.org/10.1016/j.jaci.2024.08.013.

Rahman, O., Rahman, Md.M., Maniruzzaman, M., 2024. Removal of dye and heavy metals from industrial wastewater by activated charcoal-banana rachis cellulose nanocrystal composites filter. Int. J. Environ. Anal. Chem. 104, 1478–1496. https://doi.org/10.1080/03067319.2022.2039647.

Raju, S., Woo, H., Koehler, K., Fawzy, A., Liu, C., Putcha, N., Balasubramanian, A., Peng, R.D., Lin, C.T., Lemoine, C., Wineke, J., Berger, R.D., Hansel, N.N., McCormack, M.C., 2023. Indoor air pollution and impaired cardiac autonomic function in chronic obstructive pulmonary disease. Am. J. Respir. Crit. Care Med. 207, 721–730. https://doi.org/10.1164/rccm.202203-0523OC.

Rana, A.K., Mostafavi, E., Alsanie, W.F., Siwal, S.S., Thakur, V.K., 2023. Cellulose-based materials for air purification: a review. Ind. Crop. Prod. 194, 116331. https://doi.org/10.1016/j.indcrop.2023.116331.

Sadegh, F., Sadegh, N., Wongniramaikul, W., Apiratikul, R., Choodum, A., 2024. Adsorption of volatile organic compounds on biochar: a review. Process Saf. Environ. Prot. 182, 559–578. https://doi.org/10.1016/j.psep.2023.11.071.

Saraga, D.E., Querol, X., Duarte, R.M.B.O., Aquilina, N.J., Canha, N., Alvarez, E.G., Jovasevic-Stojanovic, M., Bekö, G., Byčenkienė, S., Kovacevic, R., Plauškaitė, K., Carslaw, N., 2023. Source apportionment for indoor air pollution: current challenges and future directions. Sci. Total Environ. 900, 165744. https://doi.org/10.1016/j.scitotenv.2023.165744.

Sawatdee, S., Botalo, A., Noinonmueng, T., Posoknistakul, P., Intra, P., Pongchaikul, P., Charnnok, B., Chanlek, N., Laosiripojana, N., Wu, K.C.W., Sakdaronnarong, C., 2025. Fabrication of multilayer cellulose filters isolated from natural biomass for highly efficient air filtration for replacement of synthetic HEPA filters. Process. Saf. Environ. Prot. 194, 216–230. https://doi.org/10.1016/j.psep.2024.12.007.

Sreńscek-Nazzal, J., Kamińska, A., Serafin, J., Michalkiewicz, B., 2024. Chemical activation of banana peel waste-derived biochar using KOH and urea for CO2 capture. Materials 17, 872. https://doi.org/10.3390/ma17040872.

Sujiono, E.H., Zabrian, D., Zurnansyah, Mulyati, Zharvan, V., Samnur N.A., Humairah, 2022. Fabrication and characterization of coconut shell activated carbon using variation chemical activation for wastewater treatment application. Results Chem. 4, 100291. https://doi.org/10.1016/j.rechem.2022.100291.

Tiwari, A., Sanjog, J., 2025. Morphological, structural, and thermal properties of cellulose nanocrystals extracted from Indian water chestnut shells (agricultural waste). Next Materials 8, 100653. https://doi.org/10.1016/j.nxmate.2025.100653.

Tonu, N.T., Kundu, S., Islam, Md.M., Dhar, P.K., Khandaker, T., Anik, M.A.A.M., Dutta, S.K., Hasan, Md.K., Hossain, M.S., 2024. Fabrication of waste biomass-derived KOH activated carbon for enhanced CO 2 capture. New J. Chem. 48, 20212–20224. https://doi.org/10.1039/D4NJ04495A.

Vardoulakis, S., Giagloglou, E., Steinle, S., Davis, A., Sleeuwenhoek, A., Galea, K.S., Dixon, K., Crawford, J.O., 2020. Indoor exposure to selected air pollutants in the home environment: a systematic review. Int. J. Environ. Res. Public Health 17, 8972. https://doi.org/10.3390/ijerph17238972.

Xiang, W., Gan, L., Wang, Y., Yang, N., Wang, W., Li, L., Liu, Z., Feng, Y., Chen, D., Wang, R., 2025. Enhanced adsorption performance of phosphoric acid activated biochar from in-situ pre-carbonized bamboo shoot shells. Ind. Crop. Prod. 226, 120719. https://doi.org/10.1016/j.indcrop.2025.120719.

Yaghoot-Nezhad, A., Moradi, M., Rostami, M., Danaee, I., Khosravi-Nikou, M.R., 2020. Dual Z-Scheme CuO-ZnO@graphitic carbon nitride ternary nanocomposite with improved visible light-induced catalytic activity for ultrasound-assisted photocatalytic desulfurization. Energy Fuel 34. https://doi.org/10.1021/acs.energyfuels.0c02012.

Yu, Z., Wei, F., Wu, M., Lin, H., Shui, L., Jin, M., Wang, J., Tang, M., Chen, K., 2021. Association of long-term exposure to ambient air pollution with the incidence of sleep disorders: a cohort study in China. Ecotoxicol. Environ. Saf. 211, 111956. https://doi.org/10.1016/j.ecoenv.2021.111956.

Zhang, Y., Xu, X., Geng, Q., Li, Q., Li, X., Wang, Y., Tang, Z., Gao, B., Zhang, X., Chu, P.K., Huo, K., 2025. Redefining the roles of alkali activators for porous carbon. Chem. Sci. 16, 2034–2043. https://doi.org/10.1039/D4SC07145J.

Zhong, S., Zhang, X., Chen, Y., Yu, K., Huang, Y., Li, L., Ding, C., Peng, J., Zhong, M., 2024. Phoshporic acid actived biochar for efficient removal of paclobutrazol and alleviating its phytotoxicity to mung bean. Chem. Eng. Sci. 290, 119904. https://doi.org/10.1016/j.ces.2024.119904.